

Article

Iron Oxide (Fe₃O₄)-Supported SiO₂ Magnetic Nanocomposites for Efficient Adsorption of Fluoride from Drinking Water: Synthesis, Characterization, and Adsorption Isotherm Analysis

Amna Sarwar ^{1,†}, Jin Wang ^{2,*,†} , Muhammad Saqib Khan ¹ , Umar Farooq ³ , Nadia Riaz ^{1,*} , Abdul Nazir ¹, Qaisar Mahmood ^{1,*}, Abeer Hashem ^{4,5}, Al-Bandari Fahad Al-Arjani ⁴, Abdulaziz A. Alqarawi ⁶ and Elsayed Fathi Abd_Allah ⁶ 

- ¹ Department of Environmental Sciences, COMSATS University Islamabad, Abbottabad Campus, Khyber Pakhtunkhwa 22060, Pakistan; amna.sarwar@yahoo.com (A.S.); muhammadsaqib@yahoo.com (M.S.K.); abdunazeer@cuatd.edu.pk (A.N.)
- ² Department of Landscape and Architecture, School of Design, Shanghai Jiao Tong University, Shanghai 200240, China
- ³ Department of Chemistry, COMSATS University Islamabad, Abbottabad Campus, Khyber Pakhtunkhwa 22060, Pakistan; umarf@cuatd.edu.pk
- ⁴ Botany and Microbiology Department, College of Science, King Saud University, Riyadh 11451, Saudi Arabia; habeer@ksu.edu.sa (A.H.); aarjani@ksu.edu.sa (A.-B.F.A.-A.)
- ⁵ Mycology and Plant Disease Survey Department, Plant Pathology Research Institute, ARC, Giza 12511, Egypt
- ⁶ Plant Production Department, College of Food and Agricultural Sciences, King Saud University, Riyadh 11451, Saudi Arabia; alqarawi@ksu.edu.sa (A.A.A.); eabdallah@ksu.edu.sa (E.F.A.A.)
- * Correspondence: wangjin100@sjtu.edu.cn (J.W.); nadiariazz@gmail.com (N.R.); mahmoodzju@gmail.com (Q.M.)
- † First two authors equally contributed in the manuscript.



Citation: Sarwar, A.; Wang, J.; Khan, M.S.; Farooq, U.; Riaz, N.; Nazir, A.; Mahmood, Q.; Hashem, A.; Al-Arjani, A.-B.F.; Alqarawi, A.A.; et al. Iron Oxide (Fe₃O₄)-Supported SiO₂ Magnetic Nanocomposites for Efficient Adsorption of Fluoride from Drinking Water: Synthesis, Characterization, and Adsorption Isotherm Analysis. *Water* **2021**, *13*, 1514. <https://doi.org/10.3390/w13111514>

Academic Editor: Matthias Zessner

Received: 19 March 2021

Accepted: 20 April 2021

Published: 27 May 2021

Publisher's Note: MDPI stays neutral with regard to jurisdictional claims in published maps and institutional affiliations.



Copyright: © 2021 by the authors. Licensee MDPI, Basel, Switzerland. This article is an open access article distributed under the terms and conditions of the Creative Commons Attribution (CC BY) license (<https://creativecommons.org/licenses/by/4.0/>).

Abstract: This research work reports the magnetic adsorption of fluoride from drinking water through silica-coated Fe₃O₄ nanoparticles. Chemical precipitation and wet impregnation methods were employed to synthesize the magnetic nanomaterials. Moreover, the synthesized nanomaterials were characterized for physicochemical properties through scanning electron microscopy, Fourier-transform infrared spectroscopy, and X-ray powder diffraction. Screening studies were conducted to select the best iron oxide loading (0.0–1.5 wt%) and calcination temperature (300–500 °C). The best selected nanomaterial (0.5Fe-Si-500) showed a homogenous FeO distribution with a 23.79 nm crystallite size. Moreover, the optimized reaction parameters were: 10 min of contact time, 0.03 g L⁻¹ adsorbent dose, and 10 mg L⁻¹ fluoride (F⁻) concentration. Adsorption data were fitted to the Langmuir and Freundlich isotherm models. The Q_m and K_F (the maximum adsorption capacities) values were 5.5991 mg g⁻¹ and 1.869 L g⁻¹ respectively. Furthermore, accelerated adsorption with shorter contact times and high adsorption capacity at working pH was among the outcomes of this research work.

Keywords: magnetic nanoparticle; fluoride (F⁻) chemical precipitation method; wet impregnation method; Fe₃O₄-SiO₂ nanocomposites; reaction kinetics

1. Introduction

The occurrence of fluoride (F⁻) in water bodies is due to the combination of natural processes and anthropogenic activities [1]. The sources of F⁻ in water bodies include the natural weathering of fluorine minerals (fluorapatite and fluorite) and industrial activities such as mineral processing and glass production [2,3], as well as the use of phosphate fertilizers, aluminum and zinc smelters and coal mining products [4] refrigerants (freon), ceramics, Teflon™ cookware, and aerosol propellants [3,5]. The average fluorine concentration in the Earth's crust has been reported to be around 0.05–0.1% (500–1000 mg per kg). Fluorine concentrations in igneous, sedimentary, and metamorphic rocks vary from hundreds to thousands of milligrams per kilogram of water [6]. The chemical properties of

groundwater, especially with regard to the concentrations of F^- , are significantly affected as a result of contact with sedimentary carbonates [7]. Around 35 countries worldwide are facing the problem of fluoride contamination; amongst these, India, China, and some parts of Africa are badly affected [8,9].

High F^- concentrations ($>1.5 \text{ mg L}^{-1}$) have great effects on human health [10,11]. The excessive intake of F^- may result in fluorosis [12] and neurotransmitter and fetal cerebral dysfunction [1]. It may also result in crippling skeletal deformation, as well as pitting, staining, and loss of tooth enamel [13,14]. F^- was found to be effective for human health only when concentrations were within the permissible limit of 1.5 mg L^{-1} [3,5,15–17]. The intake of F^- in human body from drinking water at the level of 1.0 mg L^{-1} was found to be effective for bone development and prevent dental caries [18]. Different F^- concentrations and their health effects have been discussed previously [3]. The pathways through which F^- enters into human body are either through dermal contact or ingestion of food (vegetables, tea, etc.) and drinking water [19]. High F^- concentrations in the body mostly occur due to intake of drinking water. In food, the concentration of F^- is due to water [20].

The defluoridation of drinking water is a great challenge worldwide. The presence of fluoride (F^-) in drinking water is an important worldwide environmental issue due to its adverse and toxic effects [18,21]. The Earth's crust contains 0.06–0.09% fluorides. F^- is a member of halogen family, can only found in the form of inorganic and organic compounds known as F^- , and does not exist in an elemental form due to its specific characteristics, which include reactivity and electronegativity [4,5,22]. Various defluoridation techniques have been studied, including coagulation/precipitation (where alum and lime are used as coagulants in the Nalgonda technique), ion-exchange processes (using zeolite greensand, inorganic metallic oxides, and resins), membrane processes (reverse osmosis, nanofiltration, electrodialysis), and adsorption processes [5,23]. Adsorption processes are effective methods for the remediation of fluoride from drinking water. These methods have shown significant results, as shown by many recent studies [5,24,25]. The adsorption method has gained great attention because of its simple design, easy operation, flexibility, cost-effectiveness, and environmentally friendly characteristics [24].

Various adsorbents have been studied for the defluoridation of drinking water, including activated carbons, ores, and natural materials (clays, kaolinite, bentonite, lignite, mud, fly ash, alumina, chitosan etc.). Biosorbents (coconut shell, neem leaves, spirulina algae, blackberry, guava leaf, neem bark, and rice husk) are other examples [18]. Recently, nanoparticles (NPs) have gained increased attention due to their high surface-to-volume ratio [26]. NPs have become a part of modern life. NPs have been used in various industrial processes and commercial products such as cosmetics, coatings, construction, and environmental remediation [27,28]. These NPs can be used as adsorbents for contact with metallic species [29] since they provide substantial binding sites for interaction [30]. Magnetic NP adsorbents are efficacious in the treatment of both drinking water and wastewater due to their low cost, simplicity of use, small size, high surface-to-volume ratio, and environmental friendliness [31]. The use of such nanomaterials, combined with nanotechnology and magnetic separation methods, may result in an effective water pollution remediation technology [32].

In addition to their use in water treatment systems, they are also used in various fields for mineral separation and in magnetic storage devices and magnetic cooling systems (in refrigeration) [30,33]. Various NP-based treatment technologies have been reported for the adsorption of F^- , with a special focus on the type of nanomaterial and their behaviors at reported working pH for F^- removal [5,24].

The focus of this research was to defluoridate drinking water using silica-coated Fe_3O_4 nanoparticles as magnetic adsorbents. Magnetic nanoparticles (Fe-NP and Fe-Si-NC) were synthesized using chemical precipitation and wet impregnation methods, respectively. Detailed synthesis protocols are reported in the following subsections. The synthesis screening basically focuses on testing the performance of the synthesized nanocomposites (NCs) with different silica loading values (0–1.5 wt%) and calcination temperatures (300–500 °C). In addition, the best NC was selected for optimization against various parameters such as

adsorbent dose and initial concentration of F^- ($1\text{--}20\text{ mg L}^{-1}$). Only the selected NC was subject to a variety of characterizations. Different isotherms, including those of Langmuir and Freundlich, were employed to evaluate the adsorption processes.

2. Materials and Methods

2.1. Materials

The list of the equipment, chemicals, and reagents used for the synthesis of iron oxide nanoparticles and their silica composites is given in Table S1. All the chemicals were of analytical quality and were used without further processing.

2.2. Synthesis of Nanoparticles and Related Nanocomposites

Nanoparticle synthesis was carried out in 2 steps through the synthesis of nanoparticles (i.e., magnetic nanoparticles and SiO_2 nanoparticles) and related nanocomposites (Fe-Si). The detailed description of the synthesis is explained in the following sections.

2.2.1. Fe_3O_4 Nanoparticles

Magnetic nanoparticles (Fe-NPs) were prepared by using the most common and efficient chemical precipitation technique [34]. Two solutions were prepared to synthesize the nanoparticles as follows. For solution 1, 2.1 g of $\text{FeSO}_4 \cdot 7\text{H}_2\text{O}$ were dissolved in 40 mL of distilled water and for solution 2, 3.1 g of $\text{FeCl}_3 \cdot 6\text{H}_2\text{O}$ were dissolved in 40 mL of distilled water. Both solutions 1 and 2 were combined with continuous stirring and heated to $80\text{ }^\circ\text{C}$. The pH of solutions 1 and 2 was 7, and this was adjusted to 10 by the dropwise addition of NH_4OH (25%) along with continuous stirring until the solution become black. The solution was then filtered using Whatman filter paper. After filtration, nanoparticles were washed thrice with ethanol and then with distilled water, followed by drying overnight in an oven at $80\text{ }^\circ\text{C}$.

2.2.2. Synthesis of Calcium Carbonate Nanoparticles (Ca-NPs)

Ca-NPs were synthesized through a modified protocol described elsewhere [35]. In a typical method, 2 solutions, i.e., solution A (sodium nitrate) and solution B (calcium nitrate), were prepared. Solution A was prepared through mixing 0.1 M CaCO_3 and 0.18 M sodium nitrate solutions. The pH of solution A was controlled through a 1 M solution of sodium hydroxide. Meanwhile, solution B (1 M $\text{Ca}(\text{NO}_3)_2$) was prepared by adding a desired amount of calcium nitrate in deionized water. Solution B was added dropwise to solution A under continuous stirring at a constant temperature in a water bath. The resultant precipitates were filtered and dried at room temperature to obtain powdered Ca-NPs.

2.2.3. Synthesis of SiO_2 Nanoparticles (Si-NPs)

SiO_2 nanoparticles were prepared by using sodium silicate ($\text{Na}_2\text{SiO}_3 \cdot 9\text{H}_2\text{O}$). Firstly, the sodium silicate solution was prepared. Then it was added dropwise to a nanosized CaCO_3 suspension over 1 h along with continuous stirring. Both solutions were mixed and then kept in an oven at $80\text{ }^\circ\text{C}$. The pH was adjusted by adding HCl solution (10 wt%, pH range = 9–10). A mixture with a 1/10 molar ratio of $\text{SiO}_2/\text{CaCO}_3$ was produced. The mixture was stirred for the next 2 h, followed by filtering using Whatman[®] filter paper, rinsing with distilled water and ethanol, and finally drying at $100\text{ }^\circ\text{C}$ (in an oven). Calcination was performed at $700\text{ }^\circ\text{C}$ for 5 h to obtain core shell composite of the $\text{CaCO}_3\text{-SiO}_2$ nanoparticles. In order to fully extract CaCO_3 , the $\text{CaCO}_3\text{-SiO}_2$ composite was dissolved in HCl (10 wt%) for 12 h. The residual gel was purified and rinsed with distilled water. After rinsing the gel, the silica nanoparticles were calcined at $100\text{ }^\circ\text{C}$ for 1 h [36].

2.2.4. Fe-Si Nanocomposites (Fe-Si-NCs)

A series of Fe-Si nanocomposites with different Fe_3O_4 (Fe-NP) loading values (0.1, 0.25, 0.5, 1.0 and 1.5 wt/wt%) were fabricated employing the wet impregnation (WI) method. A detailed synthesis procedure was provided in our previous publication [37–39]. For Fe-

Si-NC synthesis, the known concentration of Fe-NPs was first dissolved in distilled water. Si-NPs (as a substrate) were added to Fe-NP solution and this was stirred continuously to homogenize the slurry (for an hour) followed by evaporation in a water bath with continuous stirring to obtain a thick paste. The raw Fe-Si-NCs were aged overnight and dried in an oven. The raw nanomaterial obtained was dried overnight, grinded into fine powder, calcined at 300 °C and 500 °C, and stored in a desiccator for further use.

2.3. Screening and Optimization Studies

Fe-Si-NCs were screened for their adsorption capacity of F⁻ against different synthesis and reaction parameters including different Fe₃O₄ loading values (wt%), calcination temperatures (300 °C, 500 °C), and contact times (minutes). The best selected Fe-Si-NC after screening was further evaluated for its performance against reaction parameters such as adsorbent dose (0–1 g L⁻¹), contact time (0–60 min), and initial fluoride concentration (1–20 mg L⁻¹). For a typical batch experiment, an adsorbent dose of 0.03 g L⁻¹ was used with a total of 50 mL of reaction volume. The reaction was carried out at a neutral pH (6.8) for a 1 h duration. Samples were collected (1 mL every 10 min) and analyzed using spectrophotometric method at 570 nm [40]. The adsorption percentages ($\eta\%$) and adsorption capacity (Q_e , mg g⁻¹) of Fe-Si-NCs were measured by the amount adsorbed (of fluoride) and estimated according to Equations (1) and (2)

$$\eta\% = \frac{C_0 - C_t}{C_0} \times 100 \quad (1)$$

$$Q_e = \frac{C_0 - C_t \times V}{M} \quad (2)$$

where C_0 and C_t (both in mg g⁻¹) are the initial and equilibrium F⁻ concentrations (at time t), respectively, V (L) is the volume of the aqueous solution, and M (g) is the mass of the adsorbent.

2.4. Adsorption Isotherms

Adsorption may be demonstrated as the separation of single-phase substances, accompanied by its application or concentration on the surface of the adsorption phase. The whole transfer process takes place until the conditions of stability have been reached. The correlation of isothermal data with mathematical or qualitative equations is desired for practical applications. In this study, 2 isotherms were used to describe experimental data, i.e., the Langmuir and Freundlich isotherms. The Langmuir isotherm explains the concept of a single adsorbate in a single molecular layer, whereas the Freundlich isotherm is used to model non-ideal adsorption on heterogeneous surfaces. Heterogeneity was caused by the presence of various functional groups on the surface, as well as the multiple adsorbent–adsorbate interactions. The linear transformation of the Langmuir isotherm model can be expressed as [29]:

$$\frac{1}{Q_e} = \left(\frac{1}{K_{ads}Q_m} \right) \times \frac{1}{C_e} + \frac{1}{Q_m} \quad (3)$$

where Q_e = amount of dye adsorbed (mg g⁻¹), C_e = equilibrium concentration (mg L⁻¹), K_{ads} = equilibrium adsorption constant (mg L⁻¹), and $Q_m = Q_e$ for complete monolayer adsorption capacity (mg g⁻¹). The Freundlich isotherm was used for non-ideal adsorption on heterogeneous surfaces. The heterogeneity arises from the presence of different functional groups on the surface, and the various adsorbent–adsorbate interactions. The Freundlich isotherm was expressed by the following empirical equation [41]:

$$Q_e = K_F \times C_e^{1/n} \quad (4)$$

The Freundlich isotherm was expressed by the following empirical equation [41]:

$$\log Q_e = \log K_F + \left(\frac{1}{n}\right) \log C_e \quad (5)$$

where K_F = the Freundlich adsorption constant ($L g^{-1}$). The Freundlich constant with n indicated how satisfactory the adsorption process was ($1/n$ is a measure of adsorption capacity).

2.5. Characterization of Fe-NPs and Fe-Si-NCs

Selected NPs and NCs were characterized to understand their physicochemical properties. Surface morphology (using scanning electron microscopy, SEM) was analyzed by taking microscopic images at various resolutions with the JSM-5910 scanning electron microscope (JEOL, Tokyo, Japan) at the Central Resource Laboratory (CRL), Peshawar. The surface chemistry of NCs and NPs (in powder form) was analyzed using Fourier-transform infrared spectroscopy (FTIR) in the range of 500 per cm to 4000 per cm. Phase analysis and crystallite size estimation were performed by XRD (X-ray Diffraction) using a powder X-ray diffractive meter (Cu $K\alpha$ radiation, $\lambda = 1.5418 \text{ \AA}$, 2θ range $0-80^\circ$, JDX-3532-JEOL, Japan) at the Material Resource Laboratory (MRL), Peshawar. The XRD spectra and Scherrer equation were used to calculate the crystallinity of the samples (Equation (6)) [42].

$$2\theta = \frac{K\lambda}{\beta \cos\theta} \quad (6)$$

where the crystallite size is ϕ , K represents the shape factor, the X-ray wavelength is λ , β is the full line width at the half-maximum height of the main intensity peak, and the Bragg angle is θ .

2.6. Statistical Analysis

Student's t -test was used to determine the statistical significance of the results.

3. Results and Discussion

3.1. Screening and Optimization Studies

The fluoride adsorption efficiency using Fe_3O_4 nanoparticles (FeO-NPs) and their nanocomposites (NCs) was analyzed. Fe_3O_4 - SiO_2 NCs (Fe-Si-NCs) were synthesized with different Fe_3O_4 loading values (0.1, 0.25, 0.5, 1.0, and 1.5% by wt%) onto silica NPs. After the synthesis of various Fe-Si-NCs, the synthesized compounds were further calcined at different calcination temperatures ($300^\circ C$ and $500^\circ C$). Results with the various studied screening and optimization parameters (Figure 1a) clearly show the increased adsorption efficiency of Fe-Si-NCs as compared to SiO_2 and Fe_3O_4 nanoparticles. In order to determine the effect of different Fe_3O_4 loading values (wt%) and calcination temperatures, experiments were carried out to evaluate the F^- adsorption (Q_e) efficiency of Fe-Si-NCs, and the corresponding results are shown in Figure 1b. It was evident that Fe_3O_4 loading on SiO_2 had an inverse relationship with F^- adsorption beyond an Fe-Si combination of 0.5, implying that the increase in silica loading resulted in decreased performance after 0.5 wt% Fe_3O_4 loading. However, the overall efficiency was almost the same (75%) for all the tested NCs. The highest amount of F^- adsorption was obtained using Fe-S-500 was 7.86 mg g^{-1} . Thus, Fe-Si-NCs at 0.5 wt% loading at a calcination temperature of $500^\circ C$ were selected as a suitable combination for further experiments using different adsorbent doses and initial fluoride concentrations.

Figure 1c depicts the effect of contact time on F^- adsorption on Fe-Si-NC-500 with various silica loading values (0.1, 0.25, 0.5, 1, and 1.5) and an initial F^- concentration of 10 mg L^{-1} . An L-shaped graph was obtained with Fe-Si-NC-500. It was evident that the maximum removal occurred within 10 min (6.86 mg g^{-1}). The results support

those of a previous study [43] showing that the equilibrium time was independent of F^- concentration, and that the maximum time required to achieve this was 15 min.

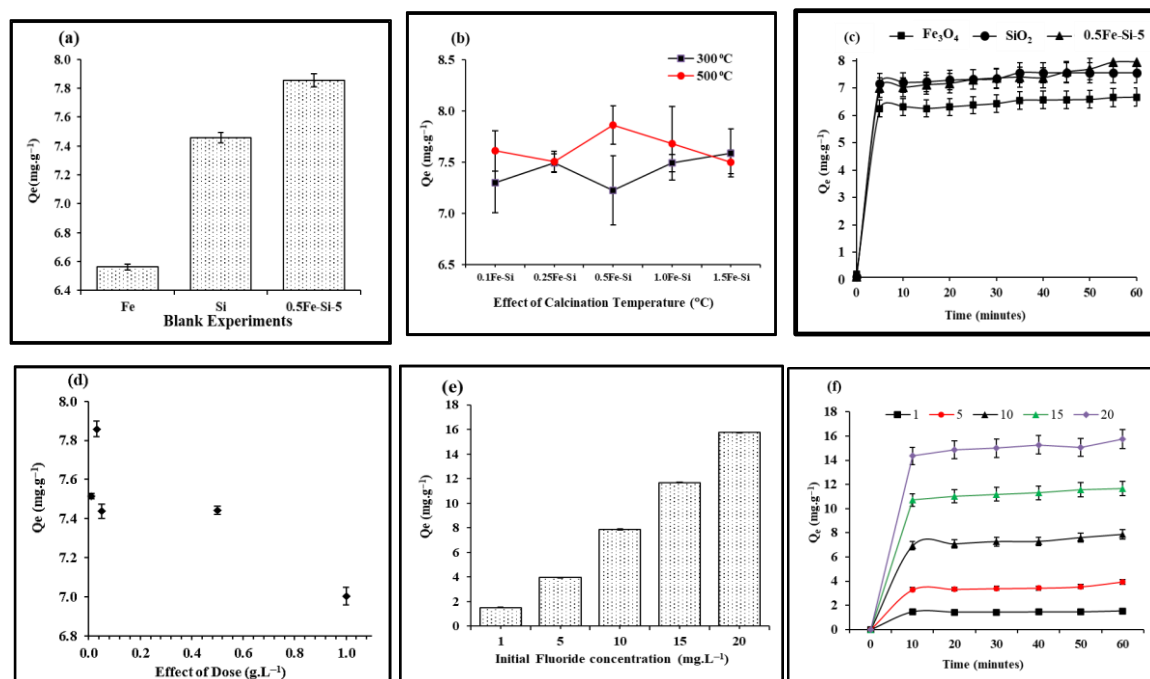


Figure 1. Screening and optimization studies of fluoride adsorption using synthesized NCs against various parameters. (a) Comparison of blanks using Fe_3O_4 , SiO_2 , and 0.5-Fe-Si-5 NCs. (b) Effect of calcination temperature using Fe_3O_4 - SiO_2 calcined at 300 °C and 500 °C. (c) Effect of contact time (min) using nanoparticles (Fe_3O_4 and SiO_2) and their best performing 0.5-Fe-Si-5 NCs. (d) Effect of adsorbent dose (0–1.0 $g L^{-1}$) using 0.5-Fe-Si-5 NCs. (e) Effect of initial fluoride concentrations ($mg L^{-1}$) using 0.5-Fe-Si-5 NCs. (f) Fluoride quantity (Q_e) adsorbed at various initial fluoride concentrations (1–20 $mg L^{-1}$) vs. time.

Based on the material employed for fluoride adsorption, different adsorption capacity values along with the contact time were reported. A minimum of 30 min for the maximum adsorption (18.7–6.35 $mg g^{-1}$) [24] has been reported for MOF-801, as for this type of material, rapid removal of F^- usually occurs when binding sites are accessible on the external layer. Since the adsorption was rapid in the beginning and then gradually slowed down before equilibrium was reached (mainly due to the weaker uptake), it was possible that the fluoride ions flowed into the porous MOF-801. According to another study, equilibrium occurred within 120 min using lanthanum-impregnated bauxite for the removal of F^- . The maximum absorption capacity of F^- was found to be 18.8 $mg g^{-1}$ [44].

One important parameter of adsorption was in relation to the impact of adsorbent doses on fluoride adsorption. Results on the impact of varying adsorbent doses (0.01, 0.03, 0.05, 0.5, and 1.0 $g L^{-1}$) with regard to fluoride removal while maintaining other parameters (F concentration and contact time) constant using 0.5 wt% Fe-Si-NC-500 are presented in Figure 1d. The dose of 0.03 $g L^{-1}$ led to the maximum fluoride adsorption (i.e., 7.86 $mg g^{-1}$). It is evident from results that as the adsorbent dose increases, the removal efficiency of the NC adsorbent decreases. There are many vacant adsorption sites on the adsorbent at the start of an adsorption operation. However, as adsorption advances, empty adsorption sites are gradually occupied. As a result, there are fewer adsorption sites available for adsorbates to bind [45]. The results presented in this study are in agreement with previously reported studies for F^- adsorption using MOF-801 showing that increasing the adsorbate dose from 0.3 to 1.5 g resulted in an increased efficiency, primarily due to an increase in the number of active sites [24]. These results are further supported by a study by [46] which showed that with an increase in adsorbent dosage above 0.02 g, adsorption

was decreased. The present study reports decreased F^- adsorption with an increase in adsorbent dose, mainly due to the blockage of active sites on the adsorbent surface [47].

Null hypothesis (H_0): $H_0 = \text{Optimum dose} = 0.03$

Alternate hypothesis (H_a): $H_a = \text{Optimum dose} \neq 0.03$

For $(n - 1)$ degree of freedom

$$t = \left(\frac{\bar{X} - \mu}{\sigma_s \sqrt{N}} \right) = t_{\text{obs}} \quad (7)$$

where σ_s is the standard deviation, \bar{X} is an average value of X , and N is sample size.

The σ_s value is ± 3.07 , while the t_{cal} value is -2.992 . However, the t value obtained from the Student's t -test table (t_{tab}) was -2.776 at a 5% level of significance for 4 df and a 2-tailed t -distribution (also known as Student's T Distribution) [48,49]. As can be seen in Figure 2 the t_{cal} value was less than t_{tab} value, so the H_0 (that the optimum dose was 0.03 g L^{-1}) was accepted.

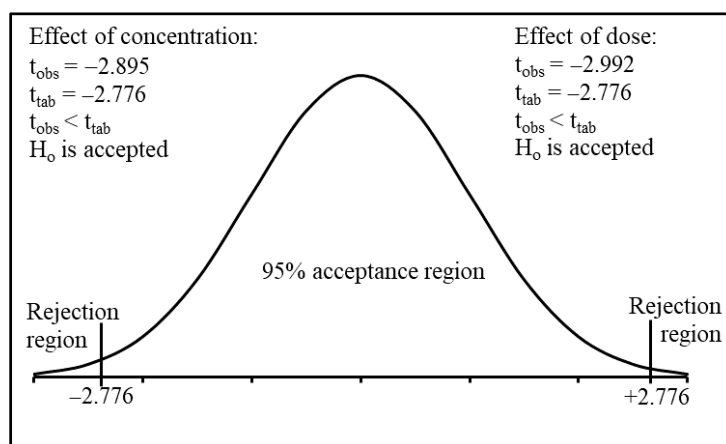


Figure 2. Probability chart for t distribution of 2-tailed test for the effect of dose and different fluoride concentrations.

Results on the fluoride quantity adsorbed against initial F^- concentration (1, 5, 10, 15, 20 mg L^{-1}) at neutral pH using 0.5 wt% $\text{Fe}_3\text{O}_4\text{-SiO}_2$ nanocomposites calcined at 500°C are shown in Figure 1e,f (concentration vs. time). The impact of the F^- concentration on F^- adsorption using 0.5 wt% of $\text{Fe}_3\text{O}_4\text{-SiO}_2$ nanocomposites was investigated, and it was found that adsorption ability increased linearly with increasing initial fluoride concentrations from 1 to 20 mg L^{-1} . It was noted that increasing F^- concentrations increased the driving force at the solid–liquid interface by increasing the adsorption power. The results revealed that the efficiency of adsorption was proportional to the initial concentration of fluoride ions. The adsorption capacity (instead of the adsorption rate) increased with increasing initial concentrations. This demonstrates that the adsorption mechanism is physio-adsorption [50,51]. Previous studies using MOF-801 support the present findings that an increase in initial F^- concentration (5.0–25 mg L^{-1}) results in an increased adsorption due to an increase in the driving force at the solid–liquid interface [24,47]. Another study conducted on the defluoridation of drinking water also supports the findings of the present study that with an increase in the initial F^- concentration an increase in adsorption capacity can be observed [52]. The increase in adsorption potential is mainly because of the variations in surface charges with increasing initial concentrations (positive for modified nano alumina and negative for F^-).

The Student's t -test was employed to compare the calculated and tabulated value for the adsorption of different F^- concentrations on a 0.03 g L^{-1} dose of nanomaterial. The null hypothesis (H_0) for the optimum concentration was 10 mg L^{-1} . The σ_s was ± 2.52 , while the t_{cal} was -3.895 ; however, the t value obtained from the Student's t -test table (t_{tab}) was

−2.776 at a 5% level of significance for 4 df and a two-tailed t-distribution [48,49]. As can be seen in Figure 2, the t_{cal} was less than the t_{tab} , so the H_0 (the optimum concentration was 10 mg L^{-1}) was accepted.

3.2. Adsorption Isotherm

To evaluate the adsorption processes, the Langmuir and Freundlich isotherms were used to analyze the experimental data and to discuss equilibrium condition of the adsorption. The Langmuir isotherm model (Figure 3b) shows the homogenous adsorbed material with the same energy on the surface, whereas the Freundlich isotherm model represents a direct relationship between Q_e and C_e (Figure 3a). This model represents non-uniform distribution of surface absorption heat from a heterogeneous surface. The Freundlich equation can be linearized, and the experimental results are plotted as $\log Q_e$ versus $\log C_e$ (Figure 3c). The Freundlich isotherm constants K_F and n were found to be 1.869 mg g^{-1} and 1.1651 L g^{-1} , respectively. Fluoride adsorption at 0.5 Fe-Si calcined at $500 \text{ }^\circ\text{C}$ was best suited to both the Langmuir model isotherm ($R^2 = 0.992$) and the Freundlich model isotherm ($R^2 = 0.995$). A high correlation coefficient was obtained for both the Langmuir and Freundlich isotherms, as shown in Figure 3b,c. The maximum adsorption capacities (Q_m) of various pollutants on $\text{Fe}_3\text{O}_4\text{-SiO}_2$ and other adsorbents are documented in the literature [53–58]. It can be summarized that $\text{Fe}_3\text{O}_4\text{-SiO}_2$ synthesized using various methods showed different adsorption capacity values at a working pH below 4. On the other hand, the present study showed promising results, with 5.5991 and 1.869 mg g^{-1} obtained as the maximum adsorption capacity values of Q_m and K_F (calculated using the Langmuir and Freundlich isotherms, respectively) at a neutral pH, without the addition of any reagent to change the reaction pH.

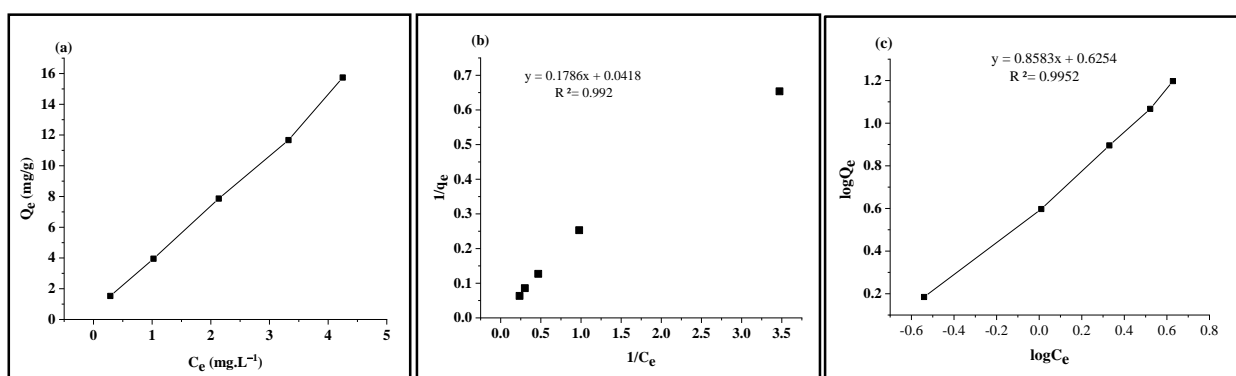


Figure 3. (a) Plot of Q_e vs. C_e (b) Langmuir (c) Freundlich adsorption isotherm of fluoride using 0.5 Fe-Si-5.

It was found that the adsorption of F^- on 0.5 Fe-Si calcined at $500 \text{ }^\circ\text{C}$ best fit into both the Langmuir model isotherm ($R^2 = 0.992$) and the Freundlich model isotherm ($R^2 = 0.995$). High correlation coefficients were obtained for both the Langmuir and Freundlich isotherm. The results of this study show consistency with both the Langmuir isotherm and the Freundlich isotherm, as shown in Figure 3b,c. The maximum adsorption capacities (Q_m) of various pollutants on the $\text{Fe}_3\text{O}_4\text{-SiO}_2$ and other adsorbents have been documented in the literature [53–58]. It can be summarized that $\text{Fe}_3\text{O}_4\text{-SiO}_2$ synthesized using various methods showed different adsorption capacity values at a working pH below 4. The obtained results showed that the studied models fitted the data in the order as follows: Freundlich ($R^2 = 0.995$) > Langmuir ($R^2 = 0.992$). A high coefficient for modeling usually means that the data follow the model. The interaction of F^- content with magnetic adsorbents is characterized as a physical adsorption phase according to the adsorption isotherm modeling. Because of their repulsion, there is no creation of a complex between the adsorbed molecules. There is a significant distinction between both adsorption isotherms applied in this study. The Freundlich isotherm is quantitative, whereas Langmuir's model

is theoretical and assumes that there is only a monomolecular layer on the surface at full coverage. This constraint does not apply to the Freundlich isotherm.

3.3. Characterization

The results for the characterization of the synthesized nanomaterials (NMs) and their composites (NCs) are discussed in this section. The characterization of the NMs and related NCs includes surface morphology (SEM) and surface chemistry (FTIR), along with crystallite size estimation (XRD). Only the best-performing NCs based on the adsorption capacities of the model pollutant were selected to analyze their physicochemical properties.

Scanning electron microscopy (SEM) and the FTIR spectrum were employed to observe the surface morphology and chemistry of the NMs and related NCs, as shown in Figure 4 (1-A represents NPs whereas 1-B represents NCs) and Figure 5, respectively. The SEM micrographs (Figure 4) of Fe_3O_4 nanoparticles and related nanocomposites after calcination at optimum operating conditions with 30,000–60,000 KX magnification are also shown. Based on the observation from SEM micrographs, NCs were seen as homogeneously distributed but noticeably agglomerated particles [59].

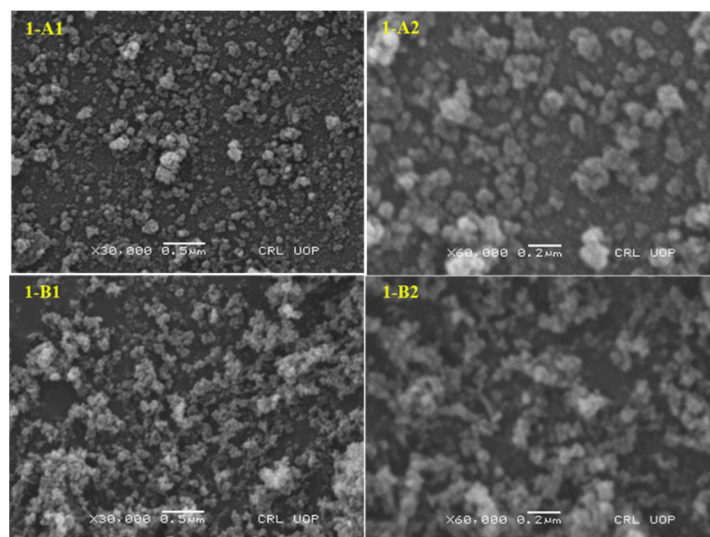


Figure 4. An SEM micrograph of Fe_3O_4 nanoparticles (1-A) and related SiO_2 nanocomposites (1-B) (calcined at 500 °C) at different resolutions.

To understand the surface chemistry of Fe_3O_4 nanoparticles and related SiO_2 nanocomposites, FTIR spectroscopy was carried out. Related results along with possible assignments for the different peaks observed along with comparison are presented in Figure 5. The comparison of the corresponding spectra revealed that for NC with SiO_2 , in addition to the adsorption of Fe-O-Fe in Fe_3O_4 around 580–590 per cm (key phase of as-synthesized particles is magnetite), new bands appeared at around 975 and 1130 per cm, and are related to Si-O-H and Si-O-Si stretching, respectively [58,60]. Broad peaks occurring at around 1622 per cm and 3450 per cm in the spectrum were attributed to O-H bond stretching and bending vibrations of water, respectively [61]. The reason for the formation of broad peak is because of the aqueous medium synthesis supporting free Fe atoms and O on the NP surface [58,62].

Phase identification and crystallite size estimation were carried out using XRD analysis. The typical XRD diffraction peaks related to the nanoparticles (Fe_3O_4 and SiO_2) and related SiO_2 nanocomposites are shown in Figure 6. Diffraction peaks were observed at 30.2°, 35.6°, 43.15°, 53.8°, 57.0°, and 63.0°, respectively, corresponding to the planes of cubic inverse spinel Fe_3O_4 (represented by a ball symbol) of 220, 311, 400, 422, 511, and 440 [59]. The incremental peak was at 26.6° for SiO_2 (shown by a square), and the majority of the peaks were comparable to those reported in Fe_3O_4 XRD patterns. As calculated using

Scherer's formula [63] the crystallite sizes of the nanoparticles (Fe_3O_4 and SiO_2) and related SiO_2 NCs were around 22.55 and 56.01 nm for Fe_3O_4 and SiO_2 NPs, respectively, and 24.88 and 23.79 nm for Fe-Si-3 and Fe-Si-5 NCs [58,59,61]. When the temperature increased, the crystallite size increased marginally, with irregular dispersion of the particle size. The increased frequency of a collision between such nanoparticle leads to an increase in the kinetic energy of the collision, giving the nanoparticles a strong tendency to overcome the potential barrier between them and clump into big particles.

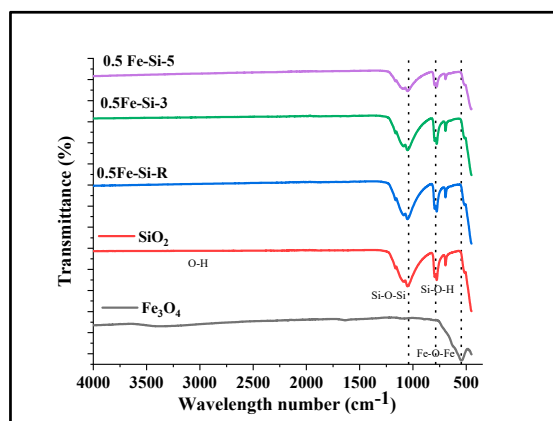


Figure 5. FTIR spectra of Fe_3O_4 nanoparticles and related SiO_2 nanocomposites (raw and calcined at 300 °C and 500 °C).

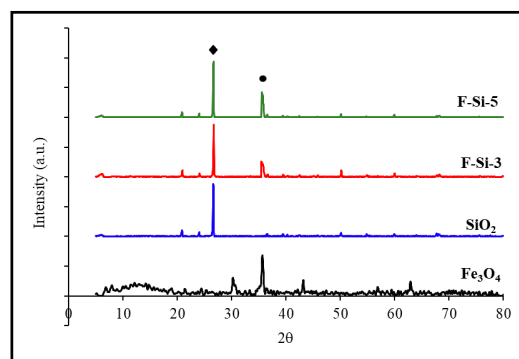


Figure 6. XRD patterns of Fe_3O_4 nanoparticles, SiO_2 , and related SiO_2 nanocomposites calcined at 300 °C and 500 °C.

When the temperature increased, the particle size became slightly bigger, and the particle size distribution was irregular. The increased frequency of collisions between the particles led to an increased kinetic energy of collisions; this gave the nanoparticles a strong tendency to overcome the potential barrier between them and agglomerate into large particles.

4. Conclusions

In conclusion, silica-coated Fe_3O_4 nanoparticle composites were successfully synthesized and used as a green magnetic nanocomposite for the efficient defluoridation of drinking water. With elevated calcination temperatures (500 °C), as the particle size increased slightly an increase in the adsorption capacity was observed, with optimum Fe_3O_4 loading at 0.5 wt%. An irregular particle size distribution along with the crystallite size was reported and verified by SEM and XRD, respectively. The investigated adsorption was maximized, with 5.599 and 1.869 mg g^{-1} obtained as the maximum adsorption capacity values in the initial 10 min for Q_m and K_F (calculated using Langmuir and Freundlich isotherms, respectively) at a neutral reaction pH. The interaction of F^- content with mag-

netic adsorbents was characterized as a physical adsorption phase according to adsorption isotherm modeling. This work showed accelerated adsorption with shorter contact times and good adsorption capacity at neutral pH as compared to reports in other studies using similar nanomaterials, without the addition of toxic solvents.

Supplementary Materials: The following are available online at <https://www.mdpi.com/article/10.3390/w13111514/s1>, Table S1: list of the equipment, chemicals, and reagents used for the synthesis of iron oxide nanoparticles and their silica composites.

Author Contributions: Conceptualization, Q.M.; methodology, N.R.; software, M.S.K.; validation, Q.M., N.R., and A.N.; formal analysis, A.S.; resources, Q.M. and J.W.; data curation, A.S.; writing—original draft preparation, A.S.; writing—review and editing, Q.M. and N.R., U.F.; supervision, Q.M. and N.R.; project administration, Q.M.; funding acquisition, A.A.A., A.H., A.-B.F.A.-A. and E.F.A.A. All authors have read and agreed to the published version of the manuscript.

Funding: This research was funded by Deanship of Scientific Research at King Saud University for funding this research group NO (RGP-271).

Acknowledgments: The authors would like to extend their sincere appreciation to the Deanship of Scientific Research at King Saud University for funding this research group NO (RGP-271) and by the Guangxi Major Projects of Science and Technology (Grant No. AA18118013, AA17202032,) from the Guangxi Science and Technology Department.

Conflicts of Interest: The authors declare no conflict of interest.

References

1. Wang, J.; Xu, W.; Chen, L.; Jia, Y.; Wang, L.; Huang, X.-J.; Liu, J. Excellent fluoride removal performance by CeO₂-ZrO₂ nanocages in water environment. *Chem. Eng. J.* **2013**, *231*, 198–205. [\[CrossRef\]](#)
2. Wang, H.; Feng, Q.; Liu, K.; Li, Z.; Tang, X.; Li, G. Highly efficient fluoride adsorption from aqueous solution by nepheline prepared from kaolinite through alkali-hydrothermal process. *J. Environ. Manag.* **2017**, *196*, 72–79. [\[CrossRef\]](#)
3. Collivignarelli, M.C.; Abbà, A.; Carnevale Miino, M.; Torretta, V.; Rada, E.C.; Caccamo, F.M.; Sorlini, S. Adsorption of Fluorides in Drinking Water by Palm Residues. *Sustainability* **2020**, *12*, 3786. [\[CrossRef\]](#)
4. Jiang, H.; Li, X.; Tian, L.; Wang, T.; Wang, Q.; Niu, P.; Chen, P.; Luo, X. Defluoridation investigation of Yttrium by laminated Y-Zr-Al tri-metal nanocomposite and analysis of the fluoride sorption mechanism. *Sci. Total Environ.* **2019**, *648*, 1342–1353. [\[CrossRef\]](#)
5. Yadav, K.K.; Gupta, N.; Kumar, V.; Khan, S.A.; Kumar, A. A review of emerging adsorbents and current demand for defluoridation of water: Bright future in water sustainability. *Environ. Int.* **2018**, *111*, 80–108. [\[CrossRef\]](#) [\[PubMed\]](#)
6. Marques, J.M.; Andrade, M.; Carreira, P.M.; Eggenkamp, H.G.M.; Graça, R.C.; Aires-Barros, L.; Antunes DA Silva, M. Chemical and isotopic signatures of Na/HCO₃/CO₂-rich geofluids, North Portugal. *Geofluids* **2006**, *6*, 273–287. [\[CrossRef\]](#)
7. Sivasankar, V.; Darchen, A.; Omine, K.; Sakthivel, R. Fluoride: A world ubiquitous compound, its chemistry, and ways of contamination. In *Surface Modified Carbons as Scavengers for Fluoride from Water*; Springer: Berlin/Heidelberg, Germany, 2016; pp. 5–32.
8. Ayooob, S.; Gupta, A.K. Performance evaluation of alumina cement granules in removing fluoride from natural and synthetic waters. *Chem. Eng. J.* **2009**, *150*, 485–491. [\[CrossRef\]](#)
9. Rasool, A.; Farooqi, A.; Xiao, T.; Ali, W.; Noor, S.; Abiola, O.; Ali, S.; Nasim, W. A review of global outlook on fluoride contamination in groundwater with prominence on the Pakistan current situation. *Environ. Geochem. Health* **2018**, *40*, 1265–1281. [\[CrossRef\]](#)
10. Shahid, M.K.; Kim, J.Y.; Shin, G.; Choi, Y. Effect of pyrolysis conditions on characteristics and fluoride adsorptive performance of bone char derived from bone residue. *J. Water Process Eng.* **2020**, *37*, 101499. [\[CrossRef\]](#)
11. Huang, L.; Yang, Z.; He, Y.; Chai, L.; Yang, W.; Deng, H.; Wang, H.; Chen, Y.; Crittenden, J. Adsorption mechanism for removing different species of fluoride by designing of core-shell boehmite. *J. Hazard. Mater.* **2020**, *394*, 122555. [\[CrossRef\]](#)
12. Meenakshi, R.C. Fluoride in drinking water and its removal. *J. Hazard. Mater.* **2006**, *137*, 456–463. [\[CrossRef\]](#)
13. Wambu, E.W.; Ambusso, W.O.; Onindo, C.; Muthakia, G.K. Review of fluoride removal from water by adsorption using soil adsorbents—An evaluation of the status. *J. Water Reuse Desalin.* **2015**, *6*, 1–29. [\[CrossRef\]](#)
14. Xu, L.; Chen, G.; Peng, C.; Qiao, H.; Ke, F.; Hou, R.; Li, D.; Cai, H.; Wan, X. Adsorptive removal of fluoride from drinking water using porous starch loaded with common metal ions. *Carbohydr. Polym.* **2017**, *160*, 82–89. [\[CrossRef\]](#)
15. Tahir, M.; Rasheed, H. Fluoride in the drinking water of Pakistan and the possible risk of crippling fluorosis. *Drink. Water Eng. Sci.* **2013**, *6*, 17–23. [\[CrossRef\]](#)
16. Fakhri, A. Application of response surface methodology to optimize the process variables for fluoride ion removal using maghemite nanoparticles. *J. Saudi Chem. Soc.* **2014**, *18*, 340–347. [\[CrossRef\]](#)
17. Pandi, K.; Periyasamy, S.; Viswanathan, N. Remediation of fluoride from drinking water using magnetic iron oxide coated hydrotalcite/chitosan composite. *Int. J. Biol. Macromol.* **2017**, *104*, 1569–1577. [\[CrossRef\]](#) [\[PubMed\]](#)

18. Sivarajasekar, N.; Paramasivan, T.; Muthusaravanan, S.; Muthukumar, P.; Sivamani, S. Defluoridation of water using adsorbents—a concise review. *J. Environ. Biotechnol. Res.* **2017**, *6*, 186–198.
19. Zhang, L.e.; Huang, D.; Yang, J.; Wei, X.; Qin, J.; Ou, S.; Zhang, Z.; Zou, Y. Probabilistic risk assessment of Chinese residents' exposure to fluoride in improved drinking water in endemic fluorosis areas. *Environ. Pollut.* **2017**, *222*, 118–125. [[CrossRef](#)] [[PubMed](#)]
20. Hussein, I.A.; Vegi, M.R. Defluoridation of drinking water using coalesced and un-coalesced mica. *Appl. Water Sci.* **2020**, *10*, 64. [[CrossRef](#)]
21. Ndé-Tchoupé, A.I.; Crane, R.A.; Mwakabona, H.T.; Noubactep, C.; Njau, K.N. Technologies for decentralized fluoride removal: Testing metallic iron-based filters. *Water* **2015**, *7*, 6750–6774. [[CrossRef](#)]
22. Rafique, T.; Naseem, S.; Bhangar, M.I.; Usmani, T.H. Fluoride ion contamination in the groundwater of Mithi sub-district, the Thar Desert, Pakistan. *Environ. Geol.* **2008**, *56*, 317–326. [[CrossRef](#)]
23. Kumari, U.; Mishra, A.; Siddiqi, H.; Meikap, B.C. Effective defluoridation of industrial wastewater by using acid modified alumina in fixed-bed adsorption column: Experimental and breakthrough curves analysis. *J. Clean. Prod.* **2021**, *279*, 123645. [[CrossRef](#)]
24. Tan, T.L.; Nakajima, H.; Rashid, S.A. Adsorptive, kinetics and regeneration studies of fluoride removal from water using zirconium-based metal organic frameworks. *RSC Adv.* **2020**, *10*, 18740–18752. [[CrossRef](#)]
25. Mahmood, Q.; Khan, M.S.; Riaz, N. Existing treatment—Globally in full scale plants. In *Pharmaceutical Wastewater Treatment Technologies: Concepts and Implementation Strategies*; Khan, N.A., Ahmed, S., Vambol, V., Vambol, S., Eds.; IWA Publishing: London, UK, 2021; p. 353. [[CrossRef](#)]
26. Saikia, J.; Sikdar, Y.; Saha, B.; Das, G. Malachite nanoparticle: A potent surface for the adsorption of xanthene dyes. *J. Environ. Chem. Eng.* **2013**, *1*, 1166–1173. [[CrossRef](#)]
27. Olabarieta, J.; Monzón, O.; Belaustegui, Y.; Alvarez, J.-I.; Zorita, S. Removal of TiO₂ nanoparticles from water by low pressure pilot plant filtration. *Sci. Total Environ.* **2018**, *618*, 551–560. [[CrossRef](#)]
28. Homaeigohar, S. Water Treatment with New Nanomaterials. *Water* **2020**, *12*, 1507. [[CrossRef](#)]
29. Khan, M.S.; Shah, J.A.; Riaz, N.; Butt, T.A.; Khan, A.J.; Khalifa, W.; Gasm, H.H.; Latifee, E.R.; Arshad, M.; Al-Naghi, A.A.A.; et al. Synthesis and Characterization of Fe-TiO₂ Nanomaterial: Performance Evaluation for RB5 Decolorization and In Vitro Antibacterial Studies. *Nanomaterials* **2021**, *11*, 436. [[CrossRef](#)]
30. Panneerselvam, P.; Morad, N.; Tan, K.A. Magnetic nanoparticle (Fe₃O₄) impregnated onto tea waste for the removal of nickel (II) from aqueous solution. *J. Hazard. Mater.* **2011**, *186*, 160–168. [[CrossRef](#)]
31. Rajput, S.; Singh, L.P.; Pittman, C.U., Jr.; Mohan, D. Lead (Pb²⁺) and copper (Cu²⁺) remediation from water using superparamagnetic maghemite (γ-Fe₂O₃) nanoparticles synthesized by Flame Spray Pyrolysis (FSP). *J. Colloid Interface Sci.* **2017**, *492*, 176–190. [[CrossRef](#)]
32. Nithya, R.; Thirunavukkarasu, A.; Sathya, A.B.; Sivashankar, R. Magnetic materials and magnetic separation of dyes from aqueous solutions: A review. *Environ. Chem. Lett.* **2021**. [[CrossRef](#)]
33. Sharma, Y.; Srivastava, V. Separation of Ni (II) ions from aqueous solutions by magnetic nanoparticles. *J. Chem. Eng. Data* **2010**, *55*, 1441–1442. [[CrossRef](#)]
34. Shah, K.H.; Ali, S.; Shah, F.; Waseem, M.; Ismail, B.; Khan, R.A.; Khan, A.M.; Khan, A.R. Magnetic oxide nanoparticles (Fe₃O₄) impregnated bentonite clay as a potential adsorbent for Cr(III) adsorption. *Mater. Res. Express* **2018**, *5*, 096102. [[CrossRef](#)]
35. Babou-Kammoe, R.; Hamoudi, S.; Larachi, F.; Belkacemi, K. Synthesis of CaCO₃ nanoparticles by controlled precipitation of saturated carbonate and calcium nitrate aqueous solutions. *Can. J. Chem. Eng.* **2012**, *90*, 26–33. [[CrossRef](#)]
36. Chen, J.-F.; Ding, H.-M.; Wang, J.-X.; Shao, L. Preparation and characterization of porous hollow silica nanoparticles for drug delivery application. *Biomaterials* **2004**, *25*, 723–727. [[CrossRef](#)]
37. Iftikhar, A.; Khan, M.S.; Rashid, U.; Mahmood, Q.; Zafar, H.; Bilal, M.; Riaz, N. Influence of metallic species for efficient photocatalytic water disinfection: Bactericidal mechanism of in vitro results using docking simulation. *Environ. Sci. Pollut. Res.* **2020**, *27*, 39819–39831. [[CrossRef](#)]
38. Riaz, N.; Hassan, M.; Siddique, M.; Mahmood, Q.; Farooq, U.; Sarwar, R.; Khan, M.S. Photocatalytic degradation and kinetic modeling of azo dye using bimetallic photocatalysts: Effect of synthesis and operational parameters. *Environ. Sci. Pollut. Res.* **2020**, *27*, 2992–3006. [[CrossRef](#)] [[PubMed](#)]
39. Riaz, N.; Kait, C.F.; Man, Z.B.; Dutta, B.K.; Ramli, R.M.; Khan, M.S. Visible Light Photodegradation of Azo Dye by Cu/TiO₂. In *Advanced Materials Research*; 2014; pp. 151–159. Available online: <https://www.scientific.net/AMR.917.151> (accessed on 15 February 2021).
40. Zazouli, M.A.; Mahvi, A.H.; Dobaradaran, S.; Barafrashtehpour, M.; Mahdavi, Y.; Balarak, D. Adsorption of fluoride from aqueous solution by modified *Azolla filiculoides*. *Adsorption* **2014**, *47*, 349–358.
41. Freundlich, H.M.F. Over the adsorption in solution. *J. Phys. Chem.* **1906**, *57*, 385–471.
42. Scherrer, P. Determination of the Internal Structure and Size of Colloidal Particles by Means of X-Rays. In *Colloid Chemistry A Textbook. Chemical Technology in Single Representations*; Springer: Berlin/Heidelberg, Germany, 1912; Available online: https://doi.org/10.1007/978-3-662-33915-2_7 (accessed on 21 April 2021).
43. Mahramanlioglu, M.; Kizilcikli, I.; Bicer, I.O. Adsorption of fluoride from aqueous solution by acid treated spent bleaching earth. *J. Fluor. Chem.* **2002**, *115*, 41–47. [[CrossRef](#)]
44. Vivek Vardhan, C.M.; Srimurali, M. Removal of fluoride from water using a novel sorbent lanthanum-impregnated bauxite. *SpringerPlus* **2016**, *5*, 1426. [[CrossRef](#)] [[PubMed](#)]
45. Al-Ghouti, M.A.; Da'ana, D.A. Guidelines for the use and interpretation of adsorption isotherm models: A review. *J. Hazard. Mater.* **2020**, *393*, 122383. [[CrossRef](#)]

46. Ahmadi, S.; Rahdar, S.; Igwegbe, C.A.; Rahdar, A.; Shafighi, N.; Sadeghfar, F. Data on the removal of fluoride from aqueous solutions using synthesized P/ γ -Fe₂O₃ nanoparticles: A novel adsorbent. *MethodsX* **2019**, *6*, 98–106. [[CrossRef](#)] [[PubMed](#)]
47. Naghizadeh, A.; Gholami, K. Bentonite and montmorillonite nanoparticles effectiveness in removal of fluoride from water solutions. *J. Water Health* **2017**, *15*, 555–565. [[CrossRef](#)] [[PubMed](#)]
48. Kothari, C.R. *Research Methodology: Methods and Techniques*; New Age International: New Delhi, India, 2004.
49. Kaushal, A.; Singh, S.K. Critical analysis of adsorption data statistically. *Appl. Water Sci.* **2017**, *7*, 3191–3196. [[CrossRef](#)]
50. Meenakshi, S.; Viswanathan, N. Identification of selective ion-exchange resin for fluoride sorption. *J. Colloid Interface Sci.* **2007**, *308*, 438–450. [[CrossRef](#)]
51. Raghav, S.; Kumar, D. Adsorption Equilibrium, Kinetics, and Thermodynamic Studies of Fluoride Adsorbed by Tetrametallic Oxide Adsorbent. *J. Chem. Eng. Data* **2018**, *63*, 1682–1697. [[CrossRef](#)]
52. Shivaprasad, P.; Singh, P.K.; Saharan, V.K.; George, S. Synthesis of nano alumina for defluoridation of drinking water. *Nano Struct. Nano Objects* **2018**, *13*, 109–120. [[CrossRef](#)]
53. Zhang, Y.; Xu, Q.; Zhang, S.; Liu, J.; Zhou, J.; Xu, H.; Xiao, H.; Li, J. Preparation of thiol-modified Fe₃O₄@SiO₂ nanoparticles and their application for gold recovery from dilute solution. *Sep. Purif. Technol.* **2013**, *116*, 391–397. [[CrossRef](#)]
54. Roto, R.; Yusran, Y.; Kuncaka, A. Magnetic adsorbent of Fe₃O₄@SiO₂ core-shell nanoparticles modified with thiol group for chloroauric ion adsorption. *Appl. Surf. Sci.* **2016**, *377*, 30–36. [[CrossRef](#)]
55. Wang, Z.; Xu, J.; Hu, Y.; Zhao, H.; Zhou, J.; Liu, Y.; Lou, Z.; Xu, X. Functional nanomaterials: Study on aqueous Hg(II) adsorption by magnetic Fe₃O₄@SiO₂-SH nanoparticles. *J. Taiwan Inst. Chem. Eng.* **2016**, *60*, 394–402. [[CrossRef](#)]
56. Ding, H.; Zhao, Y.; Duan, Q.; Wang, J.; Zhang, K.; Ding, G.; Xie, X.; Ding, C. Efficient removal of phosphate from aqueous solution using novel magnetic nanocomposites with Fe₃O₄@SiO₂ core and mesoporous CeO₂ shell. *J. Rare Earths* **2017**, *35*, 984–994. [[CrossRef](#)]
57. Yimin, D.; Jiaqi, Z.; Danyang, L.; Lanli, N.; Liling, Z.; Yi, Z.; Xiaohong, Z. Preparation of Congo red functionalized Fe₃O₄@SiO₂ nanoparticle and its application for the removal of methylene blue. *Colloids Surf. A Physicochem. Eng. Asp.* **2018**, *550*, 90–98. [[CrossRef](#)]
58. Shamsizadeh, Z.; Ehrampoush Mohammad, H.; Deghani Firouzabadi, Z.; Jasemi Zad, T.; Molavi, F.; Ebrahimi Ali, A.; Kamranifar, M. Fe₃O₄@SiO₂ magnetic nanocomposites as adsorbents for removal of diazinon from aqueous solution: Isotherm and kinetic study. *Pigment Resin Technol.* **2020**, *49*, 457–464. [[CrossRef](#)]
59. Asab, G.; Zereffa, E.A.; Abdo Seghne, T. Synthesis of Silica-Coated Fe₃O₄ Nanoparticles by Microemulsion Method: Characterization and Evaluation of Antimicrobial Activity. *Int. J. Biomater.* **2020**, *2020*, 4783612. [[CrossRef](#)] [[PubMed](#)]
60. Andrade, A.L.; Souza, D.M.; Pereira, M.C.; Fabris, J.D.; Domingues, R.Z. Synthesis and characterization of magnetic nanoparticles coated with silica through a sol-gel approach. *Cerâmica* **2009**, *55*, 420–424. [[CrossRef](#)]
61. Prabhu, Y.T.; Rao, K.V.; Kumari, B.S.; Kumar, V.S.S.; Pavani, T. Synthesis of Fe₃O₄ nanoparticles and its antibacterial application. *Int. Nano Lett.* **2015**, *5*, 85–92. [[CrossRef](#)]
62. Shagholani, H.; Ghoreishi, S.M.; Mousazadeh, M. Improvement of interaction between PVA and chitosan via magnetite nanoparticles for drug delivery application. *Int. J. Biol. Macromol.* **2015**, *78*, 130–136. [[CrossRef](#)]
63. Cullity, B.D. *Elements of X-ray Diffraction*; Addison-Wesley Publishing: Boston, MA, USA, 1956.